Fuzzy C-Mean clustering on kinetic parameter estimation with generalized linear least square algorithm in SPECT

Hon-Chit Choi [1], Lingfeng Wen [1, 2], Stefan Eberl [1, 2], Dagan Feng [1, 3]
[1]Biomedical and Multimedia Information Technology (BMIT) Group, School of Information Technologies, University of Sydney, Sydney, Australia
[2]PET and Nuclear Medicine Dept., Royal Prince Alfred Hospital, Sydney, Australia
[3]Center for Multimedia Signal Processing, Department of Electronic and Information Engineering, the Hong Kong Polytechnic University, Hong Kong

ABSTRACT

Dynamic Single Photon Emission Computed Tomography (SPECT) has the potential to quantitatively estimate physiological parameters by fitting compartment models to the tracer kinetics. The generalized linear least square method (GLLS) is an efficient method to estimate unbiased kinetic parameters and parametric images. However, due to the low sensitivity of SPECT, noisy data can cause voxel-wise parameter estimation by GLLS to fail. Fuzzy C-Mean (FCM) clustering and modified FCM, which also utilizes information from the immediate neighboring voxels, are proposed to improve the voxel-wise parameter estimation of GLLS. Monte Carlo simulations were performed to generate dynamic SPECT data with different noise levels and processed by general and modified FCM clustering. Parametric images were estimated by Logan and Yokoi graphical analysis and GLLS. The influx rate (K_1), volume of distribution (V_d) were estimated for the cerebellum, thalamus and frontal cortex. Our results show that (1) FCM reduces the bias and improves the reliability of parameter estimates for noisy data, (2) GLLS provides estimates of micro parameters (K_1-k_4) as well as macro parameters, such as volume of distribution (V_d) and binding potential (BP_1 & BP_2) and (3) FCM clustering incorporating neighboring voxel information does not improve the parameter estimates, but improves noise in the parametric images. These findings indicated that it is desirable for pre-segmentation with traditional FCM clustering to generate voxel-wise parametric images with GLLS from dynamic SPECT data.

Keywords: Dynamic SPECT, FCM Clustering, Parameter estimation

1. INTRODUCTION

Static SPECT provides images of the relative 3D distribution of the radiotracer and does not provide absolute estimates of physiologic function, such as blood flow in ml/min/g or metabolic rate in mmol/min/g. By fitting a compartment model to quantitative dynamic SPECT data, absolute physiological or biochemical parameter estimations can be achieved, which not only allow regional, but also global changes in function, such as upregulation of receptors, to be assessed. Traditionally, physiological parameters are estimated from tissue time activity curves (TTACs) derived from regions of interests drawn over relevant structures. Visualization is substantially enhanced by the generation of parametric images, where each voxel in the images is calibrated in terms of the absolute physiological parameter of interest. Parametric image generation thus requires fitting of tissue time activity curves from each voxel in the 3D data set to a kinetic model for a given input function (IF). The traditional nonlinear least square (NLS) curve fitting method can give parameter estimates with low bias and is regarded as the gold standard. However, it requires considerable computation time, depends on the quality of initial parameter estimates and can be trapped in local minima. Estimation of parameters with graphical methods such as Patlak[1], Logan[2] and Yokoi[3] plots only requires a linear least square curve fit and thus they are computationally inexpensive and are relatively insensitive to noise. However, they can only provide a limited number of parameters (typically 2) and make assumptions about the underlying model, which, if not valid for a particular application, may result in biased estimates. The generalized linear least square method (GLLS) has been shown to provide fast and computationally efficient compartment model parameter estimation [4]. GLLS has been successfully applied to PET data in the brain [4, 5], heart [6] and liver [7]. However, the high noise associated with the low sensitivity of SPECT can cause the parametric image generation by GLLS to fail due to unsuccessful fits, resulting in non-physiological parameter estimates, for a substantial fraction of the voxels in the image data.

Medical Imaging 2006: Image Processing, edited by Joseph M. Reinhardt, Josien P. W. Pluim,
Proc. of SPIE Vol. 6144, 61443Z, (2006) · 0277-786X/06/$15 · doi: 10.1117/12.653017

One of the major goals of clustering is to partition a data set into subsets such that the data in each subset are similar to each other whereas data in different clusters are dissimilar. Clustering has been applied to neuroimaging to facilitate analysis of data obtained from PET[8] as well as functional MRI[9]. We have previously demonstrated that clustering can reduce the effect of noise and improve the signal to noise ratio (SNR) in physiological parameter estimation from dynamic PET data[10]. We thus investigated the potential of GLLS with fuzzy C-Mean (FCM) clustering method[11] as a means of achieving reliable parametric image generation from noisy SPECT data. Traditional FCM does not inherently consider information contained in neighboring voxels when classifying a particular voxel. The additional information contained in neighboring voxels may improve the clustering of voxels, particularly those voxels, which due to noise differ substantially from surrounding voxels. The effect of including information from neighboring voxels in the FCM clustering was thus also investigated.

2. METHODS

2.1 Simulation data

High-count Monte Carlo simulations of the Zubal mathematical brain phantom[12] were performed using the Simset package[13] with the kinetics of the nicotinic receptor tracer 5-[^{123}I]-iodo-A-85380. A parallel hole collimator and an energy window of 20% centered around 159keV for ^{123}I were assumed. The detector module specified a simple Gaussian energy blurring model for a flat SPECT detector with an energy resolution of 10% full-width at half maximum (FWHM). Scatter and photon attenuation effects were included in the simulations. TTACs were generated from the estimated rate constants (Table 1) and the plasma time activity curve (PTAC) from the experimental data[14]. As different brain structures can have different kinetics, each brain structure was simulated separately. The composite sets of dynamic projections for all brain structures were generated by multiplying the projections of individual structures with the corresponding values from TTACs at the selected time frames. The simulated scan duration was three hours in total, divided into 36 frames: 15x1-min frames, 9x5-min frames and 12x10-min frames. The composite dynamic projection data were then scaled to typical counts which were obtained from experimental studies in order to add different realistic noise levels. The scale factor was defined as $count_{max}/count_{simul}$, where $count_{max}$ denotes the maximum count for a 5 minute frame in experimental study and it ranges from 30 to 50 and $count_{simul}$ denotes the count of a similar 5 minute frame in the simulated dynamic projection. Poisson noise was then added to these scaled projection data. The noise level will be represented by the $count_{max}$ in this study and hence noise50 is low noise (high count) data and noise30 is high noise data. Typical noisy TTACs for the 3 noise levels are shown in Figure 1 for a voxel in the cerebellum. Twenty (20) sets of dynamic projection data were generated at each noise level to allow assessment of the reliability of the parameter estimates. The dynamic projection data sets were reconstructed by the iterative OS-EM algorithm with 20 subsets and 2 iterations and without any post reconstruction filtering [15]. Attenuation correction was also applied in the iterative reconstruction. Scatter correction and compensation of detector-collimator response function were not included in the data analysis.

Table 1 Rate constants for various brain regions of interest used to simulated the dynamic SPECT data

Cortex	K_1	k_2	k_3	k_4
Cerebellum	0.275	0.063	0.029	0.035
Frontal cortex	0.277	0.059	0.038	0.037
Thalamus	0.284	0.061	0.143	0.041

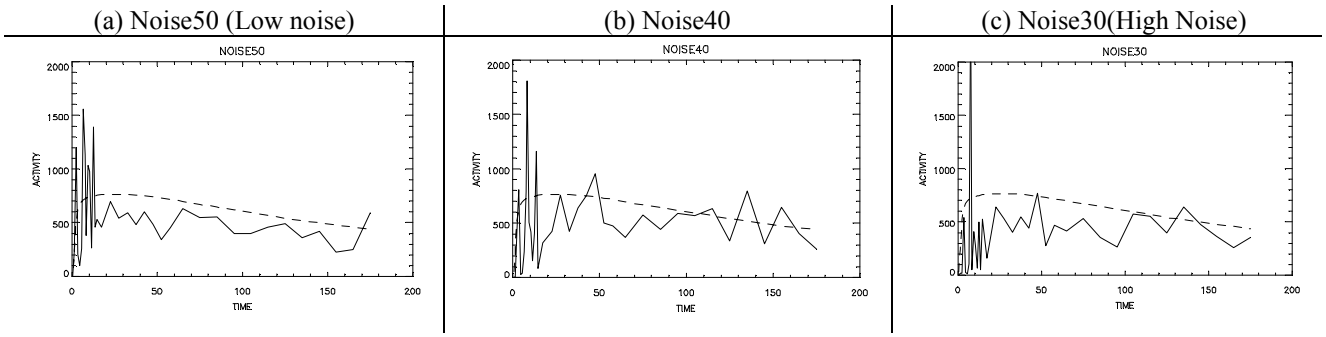

Fig.1. Typical simulated noisy curves derived from a voxel in the cerebellum for noise levels (a) $count_{max}$=50, (b) $count_{max}$=40 and (c) $count_{max}$=30. Noisy curves are represented by solid line whereas the noiseless curve is represented by the dashed line.

2.2 FCM clustering algorithm

Fuzzy c-means (FCM)[11] is a data clustering technique in which each data point is associated with every cluster by the means of fuzzy membership function. This is in contrast to hard clustering approaches where each data point belongs to one and only one cluster. In our experiment, FCM is based on the minimization of the weighted Euclidean distance function given by equation 1a. In equation 1a, x_i is the TTAC for the i-th measured voxel, c_j is the j-th centroid, n denotes the n^{th} time frame and w_D is the weight factor which equals the frame duration divided by the total scan time. Therefore, longer frames, which are more reliable, contribute more towards the distance function. In equations 1b and 1c, m>1 is the fuzziness parameter, u_{ij} is the membership value of x_i belonging to the cluster c_j. Fuzzy partitioning is carried out through an iterative optimization of the objective function with the update of membership u_{ij} and the cluster centroid c_j as shown in equation 1b and equation 1c.

The seeds for clusters were selected randomly. Memberships and centroids are then updated according to equations 1b and 1c, respectively, at the end of each iteration. The number of iteration was fixed at 7 and a fuzziness parameter m=1.1 was selected. Since our objective is to improve the quality of parameter estimation, the number of clusters is not critical and was empirically chosen to be C=16. The weighted Euclidean distance function (1a), membership update (1b) and centroid update equation (1c) for FCM are shown below.

$$D\{x_i, c_j\} = \sum_{n=1}^{N} w_{Dn} \left\| x_{in} - c_{jn} \right\|^2 \tag{1a}$$

$$u_{ij} = \frac{1}{\sum_{k=1}^{C} \left[\frac{D\{x_i, c_j\}}{D\{x_i, c_k\}} \right]^{\frac{1}{m-1}}} \quad \sum_{k=1}^{C} u_{ik} = 1 \quad \forall i \tag{1b}$$

$$c_j = \frac{\sum_{i=1}^{N} u_{ij}^m \cdot x_i}{\sum_{i=1}^{N} u_{ij}^m} \tag{1c}$$

The modified distance function shown in equation 2a was used to include information from neighboring voxels in the FCM clustering. Two regions of neighboring voxels were examined: (a) the 6 directly connected voxels (3D), and (b) the 26 voxels surrounding the target voxel in a cube, with the target voxel located at the center. In equation 2, N_k is the number of neighboring voxels. In addition we introduced a weighting function, w_N, for neighboring voxel contributions as shown in equation 2b. The weighting function increases with FCM iteration number, p, and is defined as ab^p, where a was chosen as 0.1, b as 1.7. Since a fixed number of 7 iterations is used, w_N ranges from 0.17 for the 1st iteration to 4.10 for the 7^{th} iteration. The idea behind this weighting function is that the initial clustering results are potentially less

reliable and the distance function should rely more on the voxel itself. As the results become more reliable after each iteration, the weight increases correspondingly.

$$D'\{x_i, c_j\} = D\{x_i, c_j\} + \frac{1}{N_k} \sum_{k \in Neighbor} D\{x_k, c_j\} \tag{2a}$$

$$D'\{x_i, c_j\} = D\{x_i, c_j\} + \frac{w_N}{N_k} \sum_{k \in Neighbor} D\{x_k, c_j\} \text{ where } w_N = ab^p \tag{2b}$$

2.3 Kinetic analysis

The traditional Logan and Yokoi graphical plots[3, 16] were performed to estimate parametric images of the influx rate constant, K_1, and the volume of distribution (V_d) for two-compartment model with and without FCM clustering. GLLS was applied assuming a three-compartment and four-parameter model as shown in Fig. 2 to estimate the micro-parameters, K_1 to k_4, as well as macro-parameter, V_d, with FCM clustering. The definitions of V_d for the two compartment model and three compartment model are shown in equation 3a and 3b, respectively.

The high noise intrinsic in SPECT data, especially for the voxel-wise TTACs, can result in unsuccessful estimation or physiologically meaningless parameter estimates, such as negative rate constants, with GLLS as well as other algorithms. Voxels with unsuccessful fits were set to zero.

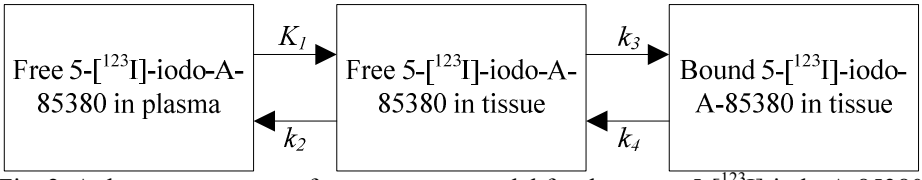

Fig. 2. A three compartment four parameter model for the tracer 5-[^{123}I]-iodo-A-85380

$$V_d = \frac{K_1}{k_2} \tag{3a}$$

$$V_d = \frac{K_1}{k_2}\left(1 + \frac{k_3}{k_4}\right) \tag{3b}$$

Regions of interest, derived from the original Zubal phantom were placed on the parametric images generated by the methods under investigation for the 3 noise levels ($count_{max}$=30 ,40 and 50). For each structure of interest (cerebellum, frontal cortex and thalamus), the mean values from the ROIs superimposed on the parametric images were compared to the known values used to simulate the data to assess bias. The reliability of the estimates was assessed by computing the standard deviations for the 20 simulated data sets at each noise level. The mean ($\overline{P}$) and standard deviation ($SD_{\overline{P}}$) were derived to estimate the percentage bias (4a) as well as the coefficient of variation (CV) (4b) according to the reference values (P_{True}) in Table 1.

$$Bias = \left| \frac{P_{True} - \overline{P}}{P_{True}} \right| X100\% \tag{4a}$$

$$CV_{\overline{P}} = \frac{SD_{\overline{P}}}{\left|\overline{P}\right|} X100\% \tag{4b}$$

2.3.1 Logan plot and Yokoi plot

The Logan and Yokoi plots linearize the differential equation describing the tracer kinetics through suitable integration and rearranging. Equations 5a and 5b represent the Logan and Yokoi plot equations, respectively. In these equations, $C_T(t)$ is the tissue concentration of the tracer, while $C_P(t)$ is the tracer plasma concentration. The volume of distribution (V_d) can then be estimated from the slope of the Logan plot (equation 5a), while K_1 is given by the intercept of the Yokoi plot (equation 5b). Thus V_d from the Logan plot and K_1 from the Yokoi plot were used to assess the performance of the graphical techniques and the effect of FCM on estimating parametric images from the graphical analysis.

$$\frac{\int_0^T C_T(t)dt}{C_T(T)} = (V_d)\left(\frac{\int_0^T C_p(t)dt}{C_T(T)}\right) - \frac{1}{k_2} \tag{5a}$$

$$\frac{C_T(T)}{\int_0^T C_p(t)dt} = (-k_2)\left(\frac{\int_0^T C_T(t)dt}{\int_0^T C_p(t)dt}\right) + K_1 \tag{5b}$$

2.3.2 Traditional 3-compartment-4-parameter GLLS

The basic theory and derivation of the unbiased GLLS for a 3-compartment and 4-parameter kinetic model has been discussed in [4]. Initial values required by GLLS are provided by linear least square (LLS) fitting. Theoretically, the measured TTAC is composed of the true TTAC and of white noise i.e.:

$$C_T(t) = C_{T(Measured)}(t) - e(t) \tag{6}$$

where e(t) represents white noise

The second order differential equation is:

$$C''_{T(Measured)}(t) = P_1 C'_p(t) + P_2 C_p(t) + P_3 C'_{T(Measured)}(t) + P_4 C_{T(Measured)}(t) \tag{7}$$

where $P_1=K_1$, $P_2=K_1(k_3+k_4)$, $P_3= k_2+k_3+k_4$, $P_4= k_2 k_4$.

For LLS, integrating the equation (7) gives,

$$C_{T(Measured)}(t) = P_1\int_0^t C_p(t)dt + P_2\int_0^t\int_0^t C_p(t)dt^2 + P_3\int_0^t C_{T(Measured)}(t)dt + P_4\int_0^t\int_0^t C_{T(Measured)}(t)dt^2 \tag{8}$$

Digitizing equation (8) at t_n (n=1,2,...,N) leads to the sampled equation which can be expressed as:

$$y = X\vartheta_{LLS-3C-4P} \tag{9}$$

where

$$y = \begin{bmatrix} c_T(t_1) \\ c_T(t_2) \\ \vdots \\ c_T(t_n) \end{bmatrix} \quad X = \begin{bmatrix} \int_0^{t_1} C_p(t)dt & \int_0^{t_1}\int_0^{t_1} C_p(t)dt^2 & \int_0^{t_1} C_{T(Measured)}(t)dt & \int_0^{t_1}\int_0^{t_1} C_{T(Measured)}(t)dt^2 \\ \int_0^{t_2} C_p(t)dt & \int_0^{t_2}\int_0^{t_2} C_p(t)dt^2 & \int_0^{t_2} C_{T(Measured)}(t)dt & \int_0^{t_2}\int_0^{t_2} C_{T(Measured)}(t)dt^2 \\ \vdots & \vdots & \vdots & \vdots \\ \int_0^{t_N} C_p(t)dt & \int_0^{t_N}\int_0^{t_N} C_p(t)dt^2 & \int_0^{t_N} C_{T(Measured)}(t)dt & \int_0^{t_N}\int_0^{t_N} C_{T(Measured)}(t)dt^2 \end{bmatrix}$$

snd $\vartheta_{LLS-3C-4P}=[P_1, P_2, P_3, P_4]^T$.

Since the measured TTACs contain measurement noise, the estimates from (9) are biased even though the direct measurement noise is white because there exist linear combinations of the integrations of white noise in the matrix X. Thus, the noise is colored.

GLLS can offer unbiased estimation, as follows:
Taking Laplace Transform of (7) and rearranging gives,

$$C_{T(Measured)}(s) = \frac{(sP_1 + P_2)C_p(s)}{(s^2 - sP_3 - P_4)} \tag{10}$$

Substituting (10) to (6) and rearranging gives,

$$s^2 C_T(s) = sP_1 C_p(s) + P_2 C_p(s) + sP_3 C_T(s) + P_4 C_T(s) - (s^2 - sP_3 - P_4)E(s) \tag{11}$$

As can be seen in equation (10), the noise term is colored even though the direct measurement noise itself is white. Consequently, it is necessary to whiten the colored noise in order to obtain unbiased estimation. If $\hat{P}_3 \cong P_3$ and $\hat{P}_4 \cong P_4$, where $\hat{P}_3$ and $\hat{P}_4$ are the estimated P_3 and P_4 from previous iteration respectively, the colored noise will be whitened and the estimates obtained are unbiased.

$$\frac{s^2 C_T(s)}{(s^2 - s\hat{P}_3 - \hat{P}_4)} = \frac{sP_1 C_p(s)}{(s^2 - s\hat{P}_3 - \hat{P}_4)} + \frac{P_2 C_p(s)}{(s^2 - s\hat{P}_3 - \hat{P}_4)} + \frac{sP_3 C_T(s)}{(s^2 - s\hat{P}_3 - \hat{P}_4)} + \frac{P_4 C_T(s)}{(s^2 - s\hat{P}_3 - \hat{P}_4)} + \frac{(s^2 - sP_3 - P_4)}{(s^2 - s\hat{P}_3 - \hat{P}_4)} E(s)$$

Rearranging the above as below (for simplicity, the filtered noise term is not rewritten),

$$C_T(s) + \frac{s\hat{P}_3 C_T(s)}{(s^2 - s\hat{P}_3 - \hat{P}_4)} + \frac{\hat{P}_4 C_T(s)}{(s^2 - s\hat{P}_3 - \hat{P}_4)} = \frac{sP_1 C_p(s)}{(s^2 - s\hat{P}_3 - \hat{P}_4)} + \frac{P_2 C_p(s)}{(s^2 - s\hat{P}_3 - \hat{P}_4)} + \frac{sP_3 C_T(s)}{(s^2 - s\hat{P}_3 - \hat{P}_4)} + \frac{P_4 C_T(s)}{(s^2 - s\hat{P}_3 - \hat{P}_4)}$$

Taking inverse Laplace transform and the 3-compartment and 4-parameter GLLS can be solved as follows,

$$\vartheta_{GLLS-3C-4P} = \left[Z^T Z\right]^{-1} Z^T r \tag{12}$$

where, $t_1, t_2, \ldots, t_n$ are the corresponding times for sampling frame, $\vartheta_{GLLS\text{-}3C\text{-}4P} = [P_1, P_2, P_3, P_4]^T$,

$$r = \begin{bmatrix} c_T(t_1) + \hat{P}_3\psi_1 \otimes c_T(t_1) + \hat{P}_4\psi_2 \otimes c_T(t_1) \\ c_T(t_2) + \hat{P}_3\psi_1 \otimes c_T(t_2) + \hat{P}_4\psi_2 \otimes c_T(t_2) \\ \vdots \\ c_T(t_n) + \hat{P}_3\psi_1 \otimes c_T(t_n) + \hat{P}_4\psi_2 \otimes c_T(t_n) \end{bmatrix} Z = \begin{bmatrix} \psi_1 \otimes c_P(t_1) & \psi_2 \otimes c_P(t_1) & \psi_1 \otimes c_T(t_1) & \psi_2 \otimes c_T(t_1) \\ \psi_1 \otimes c_P(t_2) & \psi_2 \otimes c_P(t_2) & \psi_1 \otimes c_T(t_2) & \psi_2 \otimes c_T(t_2) \\ \vdots & \vdots & \vdots & \vdots \\ \psi_1 \otimes c_P(t_n) & \psi_2 \otimes c_P(t_n) & \psi_1 \otimes c_T(t_n) & \psi_2 \otimes c_T(t_n) \end{bmatrix}$$

$$\psi_1 = \frac{\lambda_2 e^{-\lambda_2 t} - \lambda_1 e^{-\lambda_1 t}}{\lambda_2 - \lambda_1}, \psi_2 = \frac{e^{-\lambda_1 t} - e^{-\lambda_2 t}}{\lambda_2 - \lambda_1} \quad \lambda_{1,2} = \frac{\hat{P}_3 \pm \sqrt{\hat{P}_3^{\,2} + 4\hat{P}_4}}{2}.$$

where $\hat{P}_3$ and $\hat{P}_4$ are estimated parameters from the previous iteration and their initial values are obtained by linear least square (LLS) fitting [4].

3. RESULTS AND DISCUSSIONS

3.1 GLLS with FCM

The percentage bias and CV for parameter estimates of K_1 and V_d are listed in Table 2 and Table 3. The plots of parameter estimates of K_1 for thalamus and V_d for cerebellum were shown in the Figure 3. There is a clear improvement in bias and CV with FCM. While without FCM clustering, the bias and CV varied considerably between the parameter estimation methods, consistent results are obtained across the methods when applied to FCM clustered data.

Unlike Logan and Yokoi plots, which are limited to estimating two parameters, GLLS applied to these data assumes a 3 compartment, 4 parameter model. Thus it is not surprising that the increased number of parameter to be estimated with GLLS leads to a higher number of unsuccessful fits for the original raw data, which is reflected by the high bias and CV for GLLS without FCM. Clustering with FCM allows GLLS to be successfully and reliably applied. This allows the appropriate, 3-compartment model to be used for the tracer and allows all the rate constants (K_1 to k_4) to be estimated as well as macro parameters, such as binding potential and V_d.

Table 2 (a)Percentage Bias, (b) Percentage CV of parameter estimates for low noise data

Bias For Parameter Estimates (%)								
Noise50	**V_d#**	**V_d##**	**V_d***	**V_d****	**K_1^**	**K_1^^**	**K_1***	**K_1****
Cerebellum	-28.2	-17.7	-52.6	-17.9	-52.4	-34.3	-81.8	-31.0
Frontal Cortex	-56.2	-49.1	-75.8	-49.0	-69.0	-50.6	-92.4	-48.7
Thalamus	-59.9	-60.7	-66.2	-61.0	-61.4	-23.7	-93.9	-18.4

CV For Parameter Estimates (%)								
Noise50	**V_d#**	**V_d##**	**V_d***	**V_d****	**K_1^**	**K_1^^**	**K_1***	**K_1****
Cerebellum	0.3	0.2	24.4	0.2	3.2	1.0	4.6	0.4
Frontal Cortex	0.4	0.5	25.7	0.5	4.3	1.2	6.4	0.6
Thalamus	1.0	3.0	188.1	2.9	11.0	2.2	18.6	1.2

Table 3 (a)Percentage Bias, (b) Percentage CV of parameter estimates for high noise data

Bias For Parameter Estimates (%)								
Noise30	**V_d#**	**V_d##**	**V_d***	**V_d****	**K_1^**	**K_1^^**	**K_1***	**K_1****
Cerebellum	-31.3	-20.1	-74.5	-20.1	-54.1	-38.3	-92.2	-33.6
Frontal Cortex	-58.4	-49.5-	-90.0	-49.3	-71.8	-52.3	-97.2	-49.5
Thalamus	-63.6	-65.0	-85.3	-65.1	-62.3	-31.3	-97.3	-25.2

CV For Parameter Estimates (%)								
Noise30	**V_d#**	**V_d##**	**V_d***	**V_d****	**K_1^**	**K_1^^**	**K_1***	**K_1****
Cerebellum	0.4	0.7	37.0	0.7	4.4	1.9	11.9	0.8
Frontal Cortex	0.5	0.2	32.2	0.3	4.2	2.0	13.2	1.0
Thalamus	0.9	2.3	108.0	2.2	11.7	2.3	23.5	1.4

Logan without FCM; ## Logan with FCM; ^ Yokoi without FCM; ^^ Yokoi with FCM;
* GLLS without FCM; ** GLLS with FCM

Fig.3 % Bias for parameter estimates, (a) V_d for cerebellum, (b) K_1 for thalamus, at different noise levels.

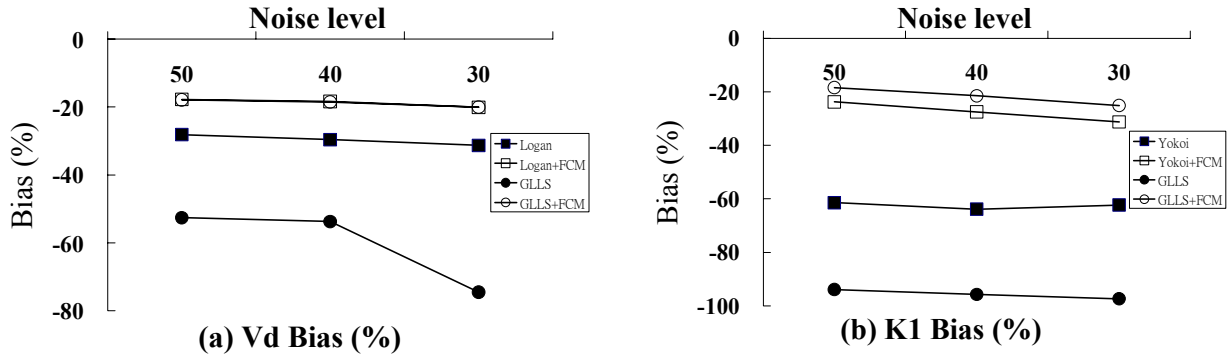

3.2 GLLS with FCM and neighborhood information

Fig. 4a and Fig.4b present parametric images for K_1 generated by GLLS+FCM without taking neighboring pixels into account (Fig. 4a) and using 26 neighboring pixels (Fig 4b). As can be seen from the figures, inclusion of neighboring pixels reduces noise and the number of spurious pixels, especially at boundaries. Table 4 and Table 5 list the percentage bias and the percentage CV of GLLS+FCM with the various neighboring pixel methods studied. Percent bias is not significantly affected by inclusion of information from neighboring pixels in the clustering. CV for the cerebellum and frontal cortex are also not affected by inclusion of neighboring voxels, but CV is increased for the thalamus with the neighboring voxel cluster methods. Even without including neighboring voxels, the CV for the thalamus is higher than that for the other structures. This is likely due to the fact that the thalamus region is quite small with high K_1 and V_d values compared to surrounding structures, thus inclusion or exclusion of peripheral voxel to the cluster can have a marked effect on the value obtained for the cluster. As more surrounding voxels can potentially contribute with the neighboring voxel clustering techniques, it is not surprising that CV increases for these techniques.

Fig.4 Parametric images for K_1 from GLLS+FCM (a) without neighboring, (b) with 26 neighboring voxels

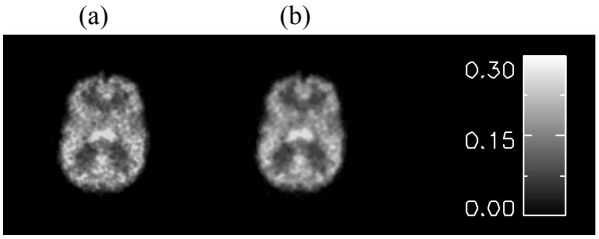

Table 4 (a) Percentage Bias, (b) Percentage CV of parameter estimates obtained by GLLS and FCM with different numbers of neighboring voxels for low noise data. The number of neighboring voxels is shown in the superscript. #: Modified weight function (W_N) used

Bias For Parameter Estimates (%)								
Noise50	V_d^0	V_d^6	V_d^{26}	$V_d^{6\#}$	K_1^0	K_1^6	K_1^{26}	$K_1^{6\#}$
Cerebellum	-17.9	-18.3	-18.8	-18.3	-31.0	-30.7	-30.8	-30.4
Frontal Cortex	-49.0	-49.5	-49.5	-49.6	-48.7	-49.0	-49.5	-49.1
Thalamus	-61.0	-60.0	-58.6	-59.6	-18.4	-19.7	-23.1	-20.7

CV For Parameter Estimates (%)								
Noise50	V_d^0	V_d^6	V_d^{26}	$V_d^{6\#}$	K_1^0	K_1^6	K_1^{26}	$K_1^{6\#}$
Cerebellum	0.2	0.3	0.6	0.4	0.4	0.9	0.9	1.1
Frontal Cortex	0.5	0.6	0.8	0.7	0.6	0.6	0.9	0.9
Thalamus	2.9	8.9	9.9	8.1	1.2	1.6	3.7	3.2

Table 5 (a) Percentage Bias, (b) Percentage CV of parameter estimates obtained by GLLS and FCM with different numbers of neighboring voxels for high noise data. The number of neighboring voxels is shown in the superscript. #: Modified weight function (W_N) used

Bias For Parameter Estimates (%)								
Noise30	V_d^0	V_d^6	V_d^{26}	$V_d^{6\#}$	K_1^0	K_1^6	K_1^{26}	$K_1^{6\#}$
Cerebellum	-20.1	-20.2	-20.6	-20.4	-33.6	-33.1	-33.3	-33.2
Frontal Cortex	-49.3	-50.0	-49.5	-50.3	-49.5	-49.7	-49.8	-50.0
Thalamus	-65.1	-65.1	-64.9	-65.0	-25.2	-24.6	-25.8	-24.6

CV For Parameter Estimates (%)								
Noise30	V_d^0	V_d^6	V_d^{26}	$V_d^{6\#}$	K_1^0	K_1^6	K_1^{26}	$K_1^{6\#}$
Cerebellum	0.7	0.6	0.8	0.4	0.8	0.9	1.0	1.1
Frontal Cortex	0.3	0.4	0.8	0.4	1.0	0.8	1.0	1.2
Thalamus	2.2	4.9	4.2	3.4	1.4	1.4	1.8	2.2

4. NEW WORK TO BE PRESENTED

As can be seen from the data in the tables, FCM clustering reduces bias in parameter estimation and improves the reliability. The Logan plot was found to be least sensitive to noise and could reliably estimate V_d even without the application of FCM clustering. However, estimation of K_1 by either Yokoi or GLLS benefited substantially from the noise reduction afforded by FCM clustering. Further, FCM clustering allowed successful application of the higher order, more general model with GLLS to provide the full set of parameter information contained in the dynamic data. While the modified FCM, which included information from neighboring voxels, did not reduce the bias further, it visible reduced the noise and spurious voxels in the parametric images.

5. CONCLUSIONS

FCM clustering and GLLS have been successfully applied to dynamic SPECT simulation data. With FCM followed by GLLS, it is possible to estimate micro parameters K_1-k_4, volume of distribution (V_d) and binding potential simultaneously with reduced bias. Thus, the potential of parameter estimation with dynamic SPECT has been demonstrated. We have also tested GLLS+FCM with various neighboring settings and found that inclusion of information from neighboring voxels during clustering does not reduce the bias further, but visibly improves the quality of the parametric images.

This work has not been submitted elsewhere.

6. ACKNOWLEDGEMENT

This work was partially supported by the Australian Research Council (ARC) and Research Grant Council of Hongkong (RGC).

7. REFERENCES

[1] C. Patlak, R. Blasberg, and J. Fenstermacher, "Graphical evaluation of blood-to-brain transfer constants from multiple-time uptake data," *J Cereb Blood Flow Metab*, vol. 3, pp. 1-7, 1983.

[2] J. Logan, J. Fowler, N. Volkow, A. Wolf, S. Dewey, D. Schlyer, R. MacGregor, R. Hitzmann, B. Bendriem, S. Gatley, and D. Christman, "Graphical analysis of reversible radioligand binding from time-activity measurements applied to [N-11C-methyl-(-)-cocaine PET studies in human subjects," *J Cereb Blood Flow Metab*, vol. 10, pp. 740-747, 1990.

[3] T. Yokoi, H. Iida, H. Itoh, and I. Kanno, "A new graphic plot analysis for cerebral blood flow and partition coefficient with iodine-123-iodoamphetamine and dynamic SPECT validation studies using oxygen-15-water and PET," *J Nucl Med*, vol. 34, pp. 498-505, 1993.

[4] D. Feng, S.-C. Huang, Z. Wang, and D. Ho, "An unbiased parametric imaging algorithm for nonuniformly sampled biomedical system parameter estimation," *Medical Imaging, IEEE Transactions on*, vol. 15, pp. 512-518, 1996.

[5] W. Cai, D. Feng, and R. Fulton, "A fast algorithm for estimating FDG model parameters in dynamic PET with an optimised image sampling schedule and corrections for cerebral blood volume and partial volume," presented at Proceedings of the 20th Annual International Conference of the IEEE Engineering in Medicine and Biology Society, 1998.

[6] K. Chen, M. Lawson, E. Reiman, A. Cooper, D. Feng, S.-C. Huang, D. Bandy, D. Ho, L.-s. Yun, and A. Palant, "Generalized linear least squares method for fast generation of myocardial blood flow parametric images with N-13 ammonia PET," *Medical Imaging, IEEE Transactions on*, vol. 17, pp. 236-243, 1998.

[7] H.-C. Choi, S. Chen, D. Feng, and K.-P. Wong, "Fast Parametric Imaging Algorithm for Dual-Input Biomedical System Parameter Estimation," *Computer Methods and Programs in Biomedicine*, pp. (Accepted).

[8] Y. Kimura, H. Hsu, H. Toyama, M. Senda, and N. M. Alpert, "Improved Signal-to-Noise Ratio in Parametric Images by Cluster Analysis," *NeuroImage*, vol. 9, pp. 554-561, 1999.

[9] C. Goutte, P. Toft, E. Rostrup, F. A. Nielsen, and L. K. Hansen, "On Clustering fMRI Time Series," *NeuroImage*, vol. 9, pp. 298-310, 1999.

[10] K.-P. Wong, D. Feng, S. R. Meikle, and M. J. Fulham, "Segmentation of dynamic PET images using cluster analysis," *Nuclear Science, IEEE Transactions on*, vol. 49, pp. 200-207, 2002.
[11] J. C. Bezdek, *Pattern recognition with fuzzy objective function algorithms*. New York: Plenum Press., 1981.
[12] I. G. Zubal, C. R. Harrell, E. O. Smith, Z. Rattner, G. Gindi, and P. B. Hoffer, "Computerized three-dimensional segmented human anatomy," *Med. Phys.*, vol. 21, pp. 299-304, 1994.
[13] T. Lewellen, R. Harrison, and S. Vannoy, "The simset program," in *Monte Carlo calculations in Nuclear Medicine, medical Science Series*. Bristol, U.K.: Institute of Physics, 1998, pp. 77-92.
[14] M. Kassiou, S. Eberl, S. R. Meikle, A. Birrell, C. Constable, M. J. Fulham, D. F. Wong, and J. L. Musachio, "In vivo imaging of nicotinic receptor upregulation following chronic (-)-nicotine treatment in baboon using SPECT," *Nucl. Med. Biol.*, vol. 28, pp. 165-175, 2001.
[15] H. M. Hudson and R. S. Larkin, "Accelerated image reconstruction using ordered subsets of projection data," *Medical Imaging, IEEE Transactions on*, vol. 13, pp. 601-609, 1994.
[16] J. Logan, "Graphical analysis of PET data applied to reversible and irreversible tracers," *Nuclear Medicine and Biology*, vol. 27, pp. 661-670, 2000.